Demonstration of an All-Microwave Controlled-Phase Gate between Far Detuned Qubits

S. Krinner,[1, *] P. Kurpiers,[1, †] B. Royer,[2, 3] P. Magnard,[1]
I. Tsitsilin,[1, 4] J.-C. Besse,[1] A. Remm,[1] A. Blais,[2, 5] and A. Wallraff[1, ‡]

[1] *Department of Physics, ETH Zurich, 8093 Zurich, Switzerland*
[2] *Institut Quantique and Départment de Physique,*
Université de Sherbrooke, Sherbrooke, Québec J1K 2R1, Canada
[3] *Department of Physics, Yale University, New Haven, Connecticut 06520, USA*
[4] *Russian Quantum Center, National University of Science and Technology MISIS, Moscow 119049, Russia*
[5] *Canadian Institute for Advanced Research, Toronto, Canada*
(Dated: June 19, 2020)

A challenge in building large-scale superconducting quantum processors is to find the right balance between coherence, qubit addressability, qubit-qubit coupling strength, circuit complexity and the number of required control lines. Leading all-microwave approaches for coupling two qubits require comparatively few control lines and benefit from high coherence but suffer from frequency crowding and limited addressability in multi-qubit settings. Here, we overcome these limitations by realizing an all-microwave controlled-phase gate between two transversely coupled transmon qubits which are far detuned compared to the qubit anharmonicity. The gate is activated by applying a single, strong microwave tone to one of the qubits, inducing a coupling between the two-qubit $|f, g\rangle$ and $|g, e\rangle$ states, with $|g\rangle$, $|e\rangle$, and $|f\rangle$ denoting the lowest energy states of a transmon qubit. Interleaved randomized benchmarking yields a gate fidelity of $97.5 \pm 0.3\%$ at a gate duration of $126\,\mathrm{ns}$, with the dominant error source being decoherence. We model the gate in presence of the strong drive field using Floquet theory and find good agreement with our data. Our gate constitutes a promising alternative to present two-qubit gates and could have hardware scaling advantages in large-scale quantum processors as it neither requires additional drive lines nor tunable couplers.

I. INTRODUCTION

Superconducting circuits making use of the concepts of circuit quantum electrodynamics [1] constitute a promising platform for quantum computing. Recently, processors containing several tens of superconducting qubits have been demonstrated [2–4]. While high-fidelity single-qubit operations with error rates below 0.1% are routinely achieved, two-qubit gate errors are typically at the percent level [5, 6], with only a few recent experiments achieving two-qubit gate errors of a few per mill [7–9]. Hence, two-qubit gates limit the performance of state-of-the-art quantum processors and a variety two-qubit gate schemes are currently explored. One typically distinguishes between two classes of approaches, flux-activated and microwave-activated gates.

The first class relies on the dynamic flux tunability of either the qubits or a separate coupling circuit. In this class gates are activated by tuning the qubits in frequency to fulfill certain resonance conditions between two-qubit states [10–14] or by parametrically modulating the qubit transition frequency [15–17]. The main benefit are short gate times, which however come at the cost of degraded coherence times or crossings with two-level-system defects [18] when tuning the qubit frequency away from its so-called sweet spot frequency, at which the qubit is first-order insensitive to flux noise [19].

In the second class of approaches the qubits are fixed in frequency and two-qubit interactions are activated using a microwave tone [20–25]. The main advantage of this approach is its potentially higher coherence when using fixed frequency qubits or frequency-tunable qubits operated at their flux sweet spot. In addition, control electronics and wiring requirements are somewhat lower as no flux control lines are needed. Instead, one resorts to the same control and pulse shaping hardware as also used for the realization of single-qubit gates. The main disadvantage of all-microwave approaches is the typically longer gate time [20–25].

The cross-resonance gate [21, 26, 27], in particular, constitutes one of the most frequently used all-microwave gates. However, for this gate to work, the detuning between the two qubits has to be smaller than the anharmonicity of the qubits. For multi-qubit devices this condition imposes stringent requirements on fabrication precision of Josephson junctions and leads to frequency crowding [28], eventually reducing gate speed and qubit addressability due to a higher sensitivity to cross talk. Here, we present an all-microwave controlled-phase gate which allows for large detunings compared to the anharmonicity. Our gate is simple and resource-friendly as it requires only a single microwave drive tone applied to one of the qubits in contrast to two drive tones [20, 25, 27], does not require re-focusing pulses during the gate [29], nor does it make use of real photons in an additional resonator [20, 24, 25]. The only requirements

are a transverse coupling between the qubits and a strong microwave drive.

II. SYSTEM AND SETUP

The Hamiltonian describing two transversally coupled transmon qubits A and B in presence of a drive on qubit A reads

$$\hat{H}/\hbar = \sum_{i=A,B} \omega_i \hat{a}_i^\dagger \hat{a}_i + \frac{\alpha_i}{2} \hat{a}_i^\dagger \hat{a}_i^\dagger \hat{a}_i \hat{a}_i$$
$$+ J\left(\hat{a}_A^\dagger \hat{a}_B + \hat{a}_A \hat{a}_B^\dagger\right) + \Omega_A(t)\left(\hat{a}_A^\dagger + \hat{a}_A\right), \quad (1)$$

with $\hat{a}_i$ ($\hat{a}_i^\dagger$) the lowering (raising) operator of qubit i, and $\Omega_A(t)$ a microwave drive applied to qubit A.

The superconducting device used in our experiment uses a frequency-tunable transmon qubit (qubit A) and a fixed-frequency transmon qubit (qubit B). The first qubit is made tunable to provide more freedom in the choice of operation frequencies, but could be at fixed frequency as well. The two qubits have frequencies $\omega_A/2\pi = 6.496\,\text{GHz}$ and $\omega_B/2\pi = 4.996\,\text{GHz}$, energy relaxation times $T_{1,A} = 7\,\mu\text{s}$ and $T_{1,B} = 20\,\mu\text{s}$, anharmonicities $\alpha_A/2\pi = -257\,\text{MHz}$ and $\alpha_B/2\pi = -271\,\text{MHz}$, and are capacitively coupled with a coupling strength $J/2\pi = 42(1)\,\text{MHz}$, see Fig. 1(a) and (b). We control the state of each qubit using amplitude and phase modulated microwave pulses [30–32], which are generated by upconverting the signals from an arbitrary waveform generator and applied to the qubits through a dedicated drive line. Prior to each experimental run we reset the qubits using the protocol introduced in [33], reducing the excited state populations of qubit A and B to 0.6% and 0.8%, respectively (see Appendix A for details).

For qubit readout, two resonators at frequencies $\omega_{r,A}/2\pi = 7.379\,\text{GHz}$ and $\omega_{r,B}/2\pi = 7.076\,\text{GHz}$ are dispersively coupled to qubit A and qubit B, respectively, with strength $g_A/2\pi = 52\,\text{MHz}$ and $g_B/2\pi = 71\,\text{MHz}$. Both resonators are coupled to a common feedline with coupling rates $\kappa_A/2\pi = 0.67\,\text{MHz}$ and $\kappa_B/2\pi = 0.63\,\text{MHz}$. We determine the $|g\rangle$, $|e\rangle$, and $|f\rangle$ state population of both qubits by applying two gated microwave tones to the feedline of the readout resonators at frequencies and powers optimized for qutrit readout [34]. The transmitted signal is amplified at 10 mK by a traveling wave parametric amplifier [35] and at 4 K by a high-electron-mobility transistor amplifier. At room temperature the signal is further amplified, split into two paths, which are separately down-converted using an I-Q mixer, digitized using an analog-to-digital converter, digitally down-converted and processed using a field programmable gate array [36]. We extract the qutrit populations of each transmon using single-shot readout. We record each measurement trace 2000 (4000) times for all characterization (randomized benchmarking) experiments and account for readout errors [37, 38] (see Appendix A).
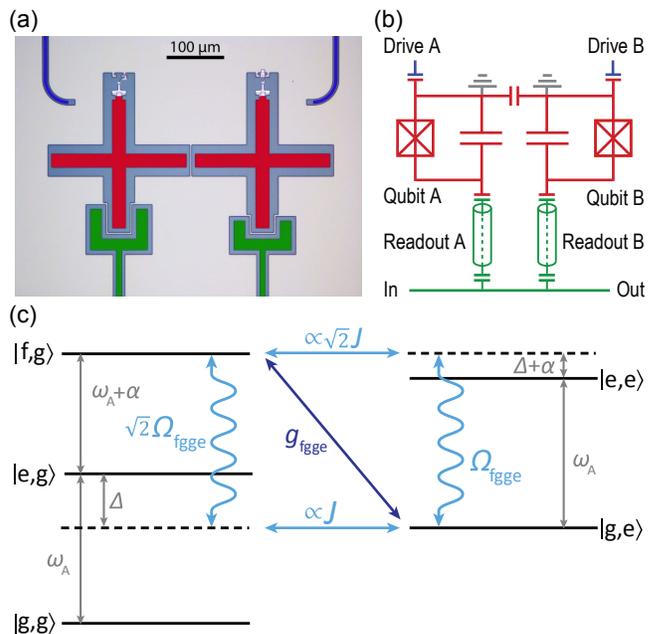

FIG. 1. Device and gate scheme. (a) Micrograph and (b) circuit diagram of the core elements of the sample. Each of the two capacitively coupled transmon qubits (red) is coupled to an individual readout resonator (green) and drive line (blue). (c) Schematic of the energy-level diagram of qubit A with qubit B in the $|g\rangle$ state (left) and in the $|e\rangle$ state (right). Virtual states are indicated by dashed lines.

III. GATE CONCEPT

Our gate exploits a Raman transition between the two-qubit states $|f,g\rangle$ and $|g,e\rangle$. The transition is analogous to the cavity-assisted Raman transition used recently for photon shaping and remote quantum communication [38–41], qutrit reset [33, 42] and two-qubit gates [25], with the distinction that here the cavity is replaced by a second qubit. The coupling between $|f,g\rangle$ and $|g,e\rangle$ is activated by a strong microwave tone $\Omega_A(t) = \Omega_{fgge} \cos(\omega_{fgge}t)$ applied to the drive line of qubit A at a frequency corresponding to the energy difference between the two states, i. e. at $\omega_{fgge,0}/2\pi = (\omega_A + \Delta + \alpha_A)/2\pi \approx 7.739\,\text{GHz}$, with $\Delta = \omega_A - \omega_B$ and the subscript '0' labeling the unshifted transition frequency in absence of a drive-induced ac-Stark shift on qubit A. The coupling is mediated by virtual states, which are coupled to $|f,g\rangle$ and $|g,e\rangle$ via the drive Ω_{fgge} and the direct qubit-qubit coupling J, see Fig. 1(c). The two coupling paths between $|f,g\rangle$ and $|g,e\rangle$ indicated by the light blue arrows interfere destructively and give rise to a total coupling strength of

$$g_{fgge} = \frac{\Omega_{fgge}J\alpha_A}{\sqrt{2}\Delta(\Delta + \alpha_A)}. \quad (2)$$

Due to the large detuning between the qubits, a large drive amplitude is required to reach a coupling strength
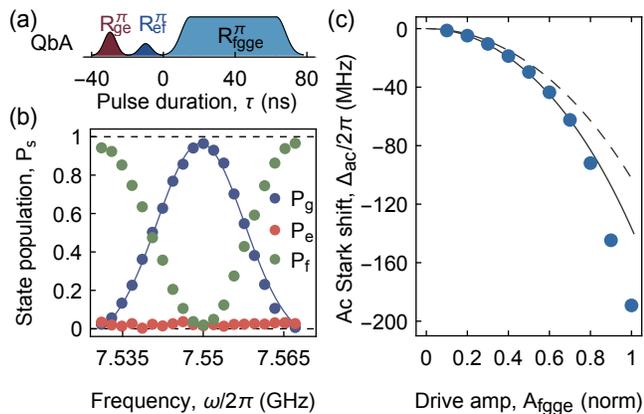
FIG. 2. Calibration of ac-Stark shift. (a) Pulse sequence applied to qubit A to resolve the fg-ge transition in a pulsed spectroscopy experiment. R_{ge}^{π} and R_{ef}^{π} label Gaussian derivative-removal-by-adiabatic-gate (DRAG) microwave pulses [30–32] for the transmon transitions $g \leftrightarrow e$ and $e \leftrightarrow f$ of angle π. R_{fgge}^{π} labels a flattop pulse on the transmon-transmon transition $fg \leftrightarrow ge$. (b) Qutrit Populations $P_{g,e,f}$ of qubit A versus the frequency $\omega/2\pi$ of a flattop fg-ge pulse with amplitude $A_{fgge} = 1.0$. The solid line is a Gaussian fit from whose center we extract the ac-Stark shift. (c) Measured ac-Stark shifts Δ_{ac} of the fg-ge transition (blue dots) versus drive amplitude A_{fgge}. The solid line is calculated from numerical simulations based on Floquet theory, while the dashed line results from simulations based on Eq. (1) in the rotating-wave approximation.

of a few MHz and thus a gate time $1/(2\,g_{fgge})$ significantly below $1\,\mu s$.

When driving the fg-ge transition for a duration which corresponds to a full round trip in the fg-ge manifold the state $|g,e\rangle$ picks up a geometric phase of π [43], thereby realizing a controlled-phase gate. Using virtual-Z gates [44], this conditional phase can be assigned to either of the computational states. We perform a virtual-Z gate on qubit B, so that the state $|e,e\rangle$ effectively picks up the phase, corresponding to flux-based implementations of controlled-phase gates which exploit the coupling between the $|e,e\rangle$ and the $|g,f\rangle$ state [10, 11, 16].

IV. GATE CALIBRATION

The fg-ge pulse is realized as a flat-top envelope with Gaussian rising and falling edges with widths $\sigma = 5\,ns$ truncated at $3\,\sigma$, carrier frequency $\omega_{fgge}/2\pi$, normalized amplitude A_{fgge}, and duration τ_{fgge}.

Due to the ac-Stark effect the fg-ge transition frequency ω_{fgge} depends on the drive amplitude Ω_{fgge}. Similar to [33], we calibrate the ac-Stark shift by preparing the qubits in the $|f,g\rangle$ state, applying the fg-ge pulse, and reading out the state of qubit A, see Fig. 2(a). For a given A_{fgge} we adjust τ_{fgge} to obtain Rabi angles close to π and measure the $|g\rangle$ state population of qubit A as a function of frequency, see Fig. 2(b). On resonance, the
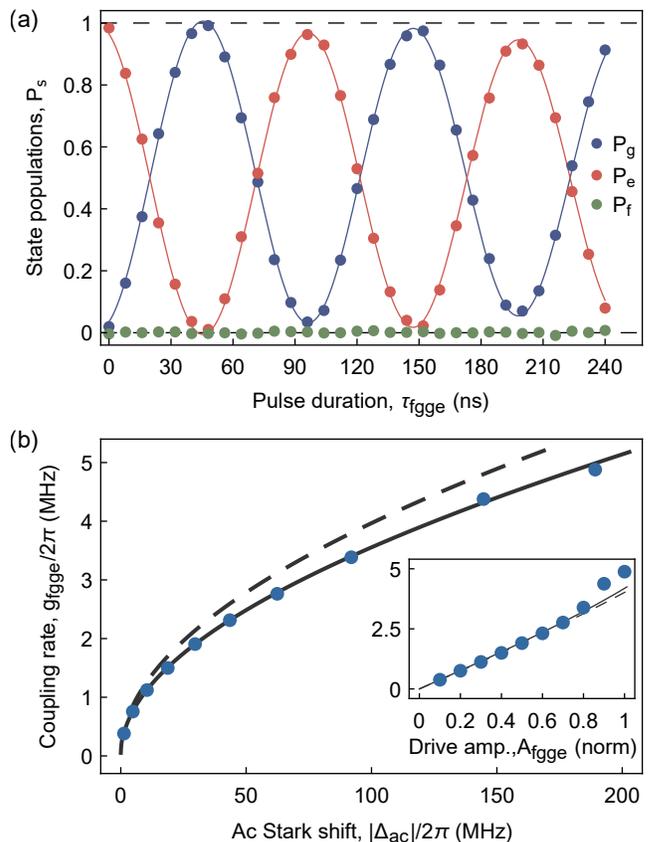

FIG. 3. Rabi oscillations. (a) Qutrit populations $P_{g,e,f}$ of qubit B versus pulse duration τ_{fgge} of a resonant flat-top fg-ge pulse with amplitude $A_{fgge} = 1.0$ corresponding to Rabi oscillations between $|f,g\rangle$ and $|g,e\rangle$. The initially prepared state is $|ge\rangle$. Solid lines are exponentially decaying sinusoidal fits. (b) Extracted coupling strength g_{fgge} vs. drive-induced ac-Stark shift Δ_{ac}. Blue dots are experimental data. The solid line is calculated from numerical simulations based on Floquet theory, while the dashed line results from simulations for which a rotating-wave approximation has been applied to Eq. (1). Inset: Coupling strength g_{fgge} vs. drive amplitude A_{fgge}.

population transfer from $|f,g\rangle$ to $|g,e\rangle$ is maximum. We fit the resulting spectrum to a Gaussian from whose center ω_{fgge} we infer the ac-Stark shift $\Delta_{ac} = \omega_{fgge} - \omega_{fgge,0}$ of the fg-ge transition frequency. In this way we measure the dependence of Δ_{ac} on A_{fgge}, see Fig. 2(c). Due to the large drive amplitude, we observe deviations from a quadratic dependence [33], as discussed below.

We next measure the coupling strength g_{fgge} vs. A_{fgge} in a Rabi experiment. For a given A_{fgge}, we prepare $|g,e\rangle$, apply the fg-ge pulse at the previously determined resonance frequency for variable τ_{fgge} and measure the qutrit populations of qubit B. We fit the resulting Rabi oscillations with an exponentially decaying sinusoidal function, see Fig. 3(a) for an example with $A_{fgge} = 1.0$. The coupling strength g_{fgge} is given by half of the fitted Rabi oscillation frequencies. For the largest drive

amplitude $A_{\text{fgge}} = 1.0$ we achieve a coupling strength $g_{\text{fgge}}/2\pi = 5.0\,\text{MHz}$. We plot the extracted $g_{\text{fgge}}/2\pi$ as a function of Δ_{ac} [Fig. 3(b)] rather than the voltage amplitude A_{fgge} set at the instrument in order to be insensitive to possible nonlinearities between A_{fgge} and the drive amplitude Ω_{fgge} at qubit A, see also Appendix B.

We obtain very good agreement between data and a numerical model based on Floquet theory with independently determined parameters [solid line in Fig. 3(b)]. The model takes into account counter-rotating terms induced by the drive and the full cosine potential of the transmon qubits, see Appendix B for details. For comparison, simulations based on a rotating-wave approximation to Hamiltonian Eq. (1) fail to accurately describe our data [dashed line in Fig. 3(b)]. Due to the large drive amplitude (for $A_{\text{fgge}} = 1$ we estimate $\Omega_{\text{fgge}}/\omega_{\text{fgge}} \sim 0.15$) counter-rotating terms in the Hamiltonian are important. For completeness, we also plot g_{fgge} *vs.* A_{fgge} [Fig. 3(b) inset]. For this data as well as for the data Δ_{ac} *vs.* A_{fgge} presented in Fig. 2(c) we observe deviations from theory for $A_{\text{fgge}} > 0.7$, which we attribute to a non-linearity between A_{fgge} and the effective drive amplitude Ω_{fgge} at qubit A, see Appendix B.

To implement a controlled-phase gate it is important to take into account the dispersive always-on coupling of the qubits. In the dispersive approximation $\Delta \gg J$ the exchange coupling term in Eq. (1) transforms into $\chi \hat{a}_A^\dagger \hat{a}_A \hat{a}_B^\dagger \hat{a}_B$, with $\chi = 2J^2(\alpha_A + \alpha_B)/[(\Delta+\alpha_A)(\Delta-\alpha_B)]$ [11]. From a Ramsey experiment we determine $\chi/2\pi = -0.83(1)\,\text{MHz}$, in agreement with the calculated value of -0.85(4) MHz and comparable to the values found in Ref. [11]. Hence, the $|e,e\rangle$ state acquires not only a conditional geometric phase ϕ_{fgge} due to the rotation in the $|fg\rangle$-$|ge\rangle$ subspace (assuming a virtual-Z gate on qubit B), but also a conditional dynamical phase ϕ_{zz} due to the disperse always-on coupling of the qubits. As a result, ϕ_{fgge} has to be smaller than π. Under the constraint of full population recovery into the computational subspace, this is achieved by driving the fg-ge transition slightly off-resonantly at a frequency $\omega_{\text{fgge}} + \Delta_{\text{fgge}}$, with Δ_{fgge} the detuning between the drive and the fg-ge transition frequency, see Appendix C. We measure the corresponding Rabi oscillations as a function of Δ_{fgge} for $A_{\text{fgge}} = 1.0$ and obtain the characteristic Chevron-like pattern shown in Fig. 4(a).

While the dispersive coupling can be taken into account in the calibration of the gate, we note that it leads to coherent errors in multi-qubit settings [45]. Possible mitigation strategies without compromising gate time include reducing the transversal coupling strength while increasing the drive strength, making use of dynamical decoupling techniques [46–49], combining qubits with opposite anharmonicity since $\chi \propto \alpha_A + \alpha_B$ [50], and driving the fg-ge transition off-resonantly during idle times, which allows for adjusting and canceling the dispersive interaction [51].

To calibrate the controlled-phase gate we follow a two-step procedure. First, we measure the conditional phase
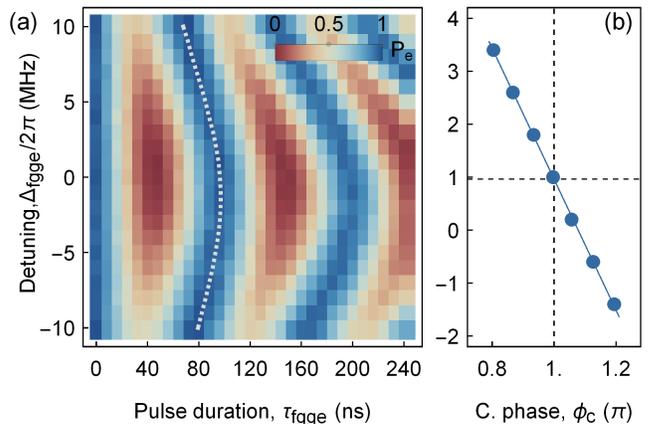

FIG. 4. (a) Excited state population P_e of qubit B as a function of pulse duration τ_{fgge} and detuning Δ_{fgge} of the fg-ge drive tone. The dashed line indicates the extracted times for which the population recovery in the computational subspace is maximum. (b) Conditional phase ϕ_c versus detuning Δ_{fgge} extracted from Ramsey experiments. Horizontal and vertical dashed lines indicate the parameters for which $\phi_c = \pi$.

$\phi_c = \phi_{\text{fgge}} + \phi_{\text{zz}}$ as a function of Δ_{fgge}. For this purpose, we extract the pulse durations τ_{fgge} for which qubit B is back in the $|e\rangle$ state, see dashed line in Fig. 4(a). This condition corresponds to minimum $|f\rangle$ level population of qubit A and therefore to maximum population recovery into the computational subspace. We then measure ϕ_c using a Ramsey experiment on qubit B while driving the fg-ge transition on qubit A, which is prepared in either $|g\rangle$ or $|e\rangle$. The difference between the phases extracted from both measurements yields ϕ_c, see Fig. 4(b). From a linear fit to the data we extract the detuning $\Delta_{\text{fgge},\pi}/2\pi = 0.962\,\text{MHz}$ which yields $\phi_c = (1.00\pm0.01)\pi$. The second step consists of calibrating the single-qubit phases $\phi_{s,i}$ with $i = A, B$, which are affected by the fg-ge drive induced ac-Stark effect. We measure $\phi_{s,i}$ using a Ramsey experiment on qubit i in the presence of the fg-ge pulse on qubit A and correct these phases using virtual-Z gates.

V. GATE CHARACTERIZATION

We finally characterize the gate by performing interleaved randomized benchmarking [52, 53]. We obtain a controlled-phase gate fidelity of 97.5(3)%, extracted from exponential fits of the form $A + Bp^s$ to the interleaved measurement and to a reference measurement, see red and blue data points in Fig. 5(a) respectively. Here, p denotes the depolarizing parameter, s is the number of applied two-qubit Clifford gates, and A, B are coefficients accounting for state preparation and measurement (SPAM) errors [53]. The fidelity of the reference measurement is 94.5(1)%.

Our qutrit readout allows us to simultaneously extract the leakage rate to the $|f\rangle$ level of both qubits. We fit
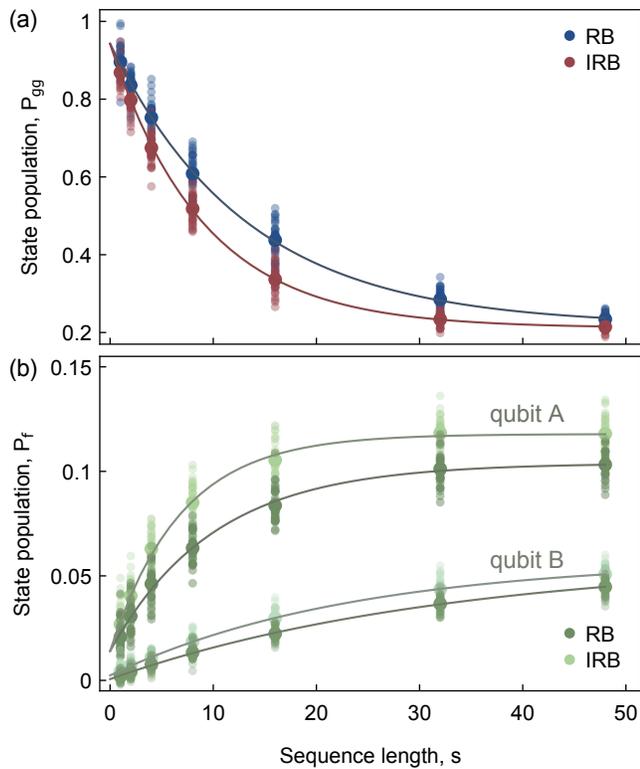
FIG. 5. Randomized benchmarking. (a) Population P_{gg} and (b) P_f versus two-qubit Clifford group gate sequence length s. The number of randomly generated sequences is 36. Solid lines in (a) are exponential fits used to extract the gate fidelity. Solid lines in (b) are fits to a rate equation model used to extract the leakage error per gate.

the observed rise in $|f\rangle$ level population P_f [Fig. 5(b)] as a function of sequence length s to a rate equation model [54] of the form $P_f(s) = p_\infty(1 - e^{-\Gamma s}) + p_0 e^{-\Gamma s}$, with p_0 the initial $|f\rangle$ level population, $p_\infty = \gamma_\uparrow/\Gamma$ the asymptotic $|f\rangle$ level population, and $\Gamma = \gamma_\uparrow + \gamma_\downarrow$ the sum of the leakage rate $\gamma_\uparrow$ and the decay rate $\gamma_\downarrow$. Subtracting the reference leakage rate $\gamma_{\uparrow,RB}$ from the leakage rate of the interleaved experiment, $\gamma_{\uparrow,IRB}$, we extract leakage errors per controlled-phase gate of $\epsilon_{l,A} = 0.7(3)\%$ and $\epsilon_{l,B} = 0.07(2)\%$ for qubit A and B, respectively. As expected, the leakage error for qubit A is significantly larger than for qubit B because only the $|f\rangle$ level of qubit A is populated during the gate.

From master equation simulations we compute an average gate fidelity of 97.5%, which is in good agreement with the measured fidelity and indicates that the gate fidelity is limited by decoherence. The numerical simulation reveal that 0.4% leakage per gate can be attributed to T_{2ef} errors on qubit A, while the remaining leakage errors are caused by other decoherence channels. In particular, due to the dressing of the states in the driven basis, different decoherence channels can contribute. Removing transmon decoherence from master equation simulations we estimate that a gate fidelity higher than 99.9% is pos-

sible without pulse optimization.

VI. SUMMARY

In summary, we have demonstrated a fast, coherence limited all-microwave controlled-phase gate between two qubits which are detuned by about six times the qubit anharmonicity. In particular, the gate imposes no constraints on the qubit-qubit detuning and is activated by a single microwave tone applied to the drive line of one of the qubits. Hence, no further resources beyond those already used for single-qubit gates are required. We therefore believe that in future multi-qubit quantum processors our gate will provide hardware scaling advantages compared to processors relying on fast flux tunability of qubits [55] and tunable coupling circuits [4]. This assumes that the relatively large always-on dispersive coupling can be mitigated without large overhead [46–51]. Finally, the engineered coupling between $|f,g\rangle$ and $|g,e\rangle$ can be used in a heralded quantum communication protocol [56], where an auxiliary qubit indicates photon loss events.
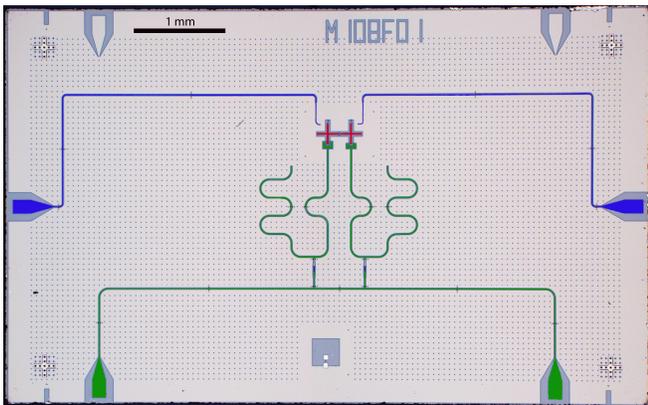
FIG. 6. False-colored micrograph of the superconducting device showing the transmon qubits in red, the readout circuit in green, and the qubit drive lines in blue.

Appendix A: Sample and Setup

The superconducting device is made of a patterned Niobium thin film on a high-resistivity Silicon substrate using standard photolithography techniques, see Fig. 6. Josephson junctions are fabricated using electron beam lithography and shadow evaporation of aluminium with lift-off. Qubit drive and fg-ge drive signals are combined before being amplified at room temperature and routed to the dilution refrigerator. We use either single sideband modulation with IQ-mixers driven by a local oscillator (LO) and an arbitrary waveform generator (AWG), or alternatively, directly synthesized drive-pulses from a high-bandwidth AWG (fAWG).

The input lines are thermalized at each temperature stage of the dilution refrigerator and are attenuated at the 4K-, CP- and BT-stages [57]. We use a superconducting coil to thread flux through the superconducting quantum-interference device (SQUID) of qubit A to tune its frequency.

The states of both transmon qubits are read out using a gated microwave tone applied to the input port of a common feed line, see Fig. 7. The output signal is routed through a circulator and a directional coupler, and amplified at 10 mK with 24 dB gain at $\omega_{r,A}/2\pi$ and 20 dB at $\omega_{r,B}/2\pi$ using a traveling wave parametric amplifier (TWPA), see Fig. 7. The TWPA is pumped at a frequency of 7.916 GHz and we obtain a phase-preserving detection efficiency of $\eta = 0.14$ for the full detection line. The signal is then further amplified by a high-electron-mobility transistor (HEMT) at 4 K and two low-noise amplifiers at room temperature. Subsequently, the signal is down-converted to 250 MHz using an analog mixer, lowpass-filtered, digitized by an analog-to-digital converter and processed by a field-programmable gate array (FPGA).

We extract the qutrit population of each transmon using single-shot readout with an averaged correct assignment probability of 92% for qubit A and 93% for qubit B.
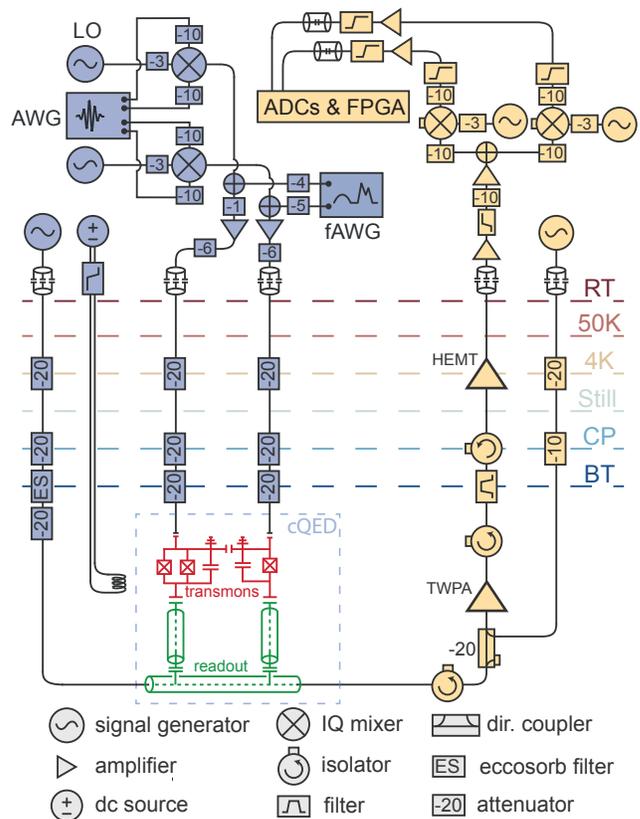

FIG. 7. Schematic of the setup. Elements shown in blue indicate input lines, elements shown in yellow indicate detection lines and dashed lines mark the stages of the dilution refrigerator (see text for details).

We obtain a maximal correct assignment probability with an integration time of $t_{m,A} = 900$ ns ($t_{m,B} = 960$ ns) and a measurement power that results in a state-dependent photon number in readout resonator A (B) of 102, 2, 86 (28, 18, 29) photons for the states $|g\rangle$, $|e\rangle$, $|f\rangle$, respectively. These photon numbers are below the critical photon numbers [58] for readout resonator A (B) of 223, 113 (77, 40) for the states $|e\rangle$, $|f\rangle$, respectively.

We extract the parameters of the readout circuit and the relevant coupling strengths from fits to transmission spectrum measurements. The coherence times and anharmonicity of the qutrits are determined in standard time-resolved measurements. All relevant device parameters are listed in Table I.

Appendix B: Calibration of AC-Stark Shift and Coupling Strength

To go beyond Eq. (2), which expresses the coupling strength g_{fgge} as a linear function of the drive amplitude Ω_{fgge}, we numerically diagonalize the system Hamiltonian in dependence on the drive amplitude. For each drive amplitude, we aim to extract both the resonant

drive frequency ω_{fgge} of the fg-ge transition and the coupling strength. In order to take into account the effect of the drive and the cosine potential of the Josephson junctions fully, we model the coupled two-transmon system in the lab frame,

$$\hat{H}_{\text{Floquet}}/\hbar = \sum_{i=A,B} 4E_{C,i}\hat{n}_i^2 - E_{J,i}\cos(\hat{\varphi}_i) \qquad (B1)$$
$$+ \tilde{J}\hat{n}_A\hat{n}_B + \Omega(t)\hat{n}_A,$$

where all transmon operators are taken in the charge basis, $\tilde{J}$ is set by the coupling capacitance between the two transmons, and $E_{C,i}$ and $E_{J,i}$ are the charging energy and Josephson energy of transmon i, respectively. We consider a drive of the form $\Omega_{\text{A}}(t) = \Omega_{\text{fgge}}\cos(\omega t)$, and find the resonance frequency $\omega_{\text{fgge}}(\Omega_{\text{fgge}})$.

We first set the drive amplitude to zero, $\Omega_{\text{fgge}} = 0$, and choose the parameters $\{E_{C,i}, E_{J,i}, \tilde{J}\}$ in order to reproduce the independently extracted parameters listed in Table I. We then perform a numerical spectroscopy experiment, and extract $g_{\text{fgge}}(\Omega_{\text{fgge}})$ and $\omega_{\text{fgge}}(\Omega_{\text{fgge}})$ for each drive amplitude Ω_{fgge} following an approach similar to Ref. [40]. Essentially, we fix Ω_{fgge} and scan the drive frequency ω, diagonalizing the Hamiltonian for different values of ω. We then extract g_{fgge} and ω_{fgge} from the anticrossing between the states closest to $(|f,g\rangle \pm |g,e\rangle)/\sqrt{2}$. We extend the numerical protocol in two major ways compared to Ref. [40]. First, we consider the Hamiltonian in the charge basis, which allows to take into account the full cosine potential of the two transmons. Due to the large drive amplitude, higher states than the $|f\rangle$ state of the transmons are populated. We obtain a maximum population of the $|h\rangle$ ($|i\rangle$) state of 30% (6%). Modeling the system Hamiltonian in the charge basis instead of taking an anharmonic oscillator basis allows to describe these states more accurately. Second, we consider the full effect of the drive and find the Floquet eigenmodes [59] of the system in the lab frame instead of performing a rotating-wave approximation (RWA) and diagonalizing a time-independent Hamiltonian in the rotating frame of the drive. This allows to accurately describe the drive since the largest amplitudes considered here correspond to a significant fraction of the drive frequency, $A_{\text{fgge}} = 1 \rightarrow \Omega_{\text{fgge}}/\omega_{\text{fgge}} \approx 0.15$.

To compare the numerical curves with the experimental data, we fit an amplitude conversion factor $A_{\text{fgge}} = C_{\text{conv}} \times \Omega_{\text{fgge}}$ over the small drive amplitude range $0 \leq A_{\text{fgge}} \leq 0.6$. While Fig. 2(c) and the inset of Fig. 3(b) show discrepancies between the data and the numerical model for $A_{\text{fgge}} > 0.7$, Fig. 3(b) does not depend on the drive amplitude and shows good agreement between the numerical (black line) and experimental data (blue dots) with independently determined parameters. Considering that the simulations agree well with the experimental data when comparing quantities not sensitive to the drive amplitude, we suggest that the discrepancies observed in Fig. 2(c) and the inset of Fig. 3(b) are due to the conversion factor between A_{fgge} and Ω_{fgge} depending on frequency, i.e. $C_{\text{conv}} = C_{\text{conv}}(\omega_{\text{fgge}})$.

This can be the case if the drive line of qubit A has a frequency-dependent response or if there are secondary coupling paths from the drive line to the qubit. We verified that the drive line section between the output of the arbitrary waveform generator instrument and the printed circuit board on which the chip is mounted has no frequency dependence beyond the weakly increasing attenuation as a function of frequency characteristic for semi-rigid microwave cables (see e.g. Fig. 13 a in [57]), which only explains a 2% deviation of C_{conv} at maximum drive amplitude compared to its low amplitude value. However, an impedance mismatch between PCB and the on-chip part of the drive line could introduce a larger frequency dependence. Considering secondary coupling paths, it is possible that in addition to the direct coupling path from drive line to qubit A, a second path is mediated by the readout resonator of qubit A, which has a frequency $\omega_{\text{r,A}}/2\pi = 7.379\,\text{GHz}$. The contribution of such a second path is expected to become larger as ω_{fgge} gets closer to $\omega_{\text{r,A}}$ and the effective Ω_{fgge} would be given by the interference of both paths.

Appendix C: Calibration of Conditional Phase

The total conditional phase $\phi_c = \phi_{\text{fgge}} + \phi_{\text{zz}}$ accumulated during the gate is a combination of the geometric phase ϕ_{fgge} and the dynamical phase $\phi_{\text{zz}} = -\chi t_g$ due to the dispersive coupling. In order to obtain a total phase of $\phi_c = \pi$, the geometric phase should consequently be adjusted to

$$\phi_{\text{fgge}} = \pi + \chi t_g. \qquad (C1)$$

This geometric phase can be computed by considering the evolution in the effective $|fg\rangle, |ge\rangle$ two-level system. Denoting the effective Pauli matrices $\tilde{X} = |fg\rangle\langle ge| + |ge\rangle\langle fg|$ and $\tilde{Z} = |fg\rangle\langle fg| - |ge\rangle\langle ge|$, we write an effective two-level Hamiltonian for the driven system

$$\hat{H}_{\text{fgge}} = g_{\text{fgge}}\tilde{X} + \frac{1}{2}\Delta_{\text{fgge}}\tilde{Z}, \qquad (C2)$$

quantity, symbol (unit)	A	B
readout resonator frequency, $\omega_{\text{r}}/2\pi$ (GHz)	7.3789	7.0762
readout resonator bandwidth, $\kappa/2\pi$ (MHz)	0.671	0.633
readout circuit dispersive shift, $\chi/2\pi$ (MHz)	0.680	0.280
qubit transition frequency, $\omega_{\text{ge}}/2\pi$ (GHz)	6.4961	4.9962
transmon anharmonicity, $\alpha/2\pi$ (MHz)	-257.4	-271.4
qubit-qubit coupling strength, $J/2\pi$ (MHz)	42 ± 1	
energy relaxation time on ge, T_{1ge} (μs)	7.7 ± 0.7	26 ± 6
energy relaxation time on ef, T_{1ef} (μs)	4.4 ± 0.5	9 ± 2
coherence time on ge, $T_{\text{2ge}}^{\text{R}}$ (μs)	10.3 ± 0.6	17 ± 4
coherence time on ef, $T_{\text{2ef}}^{\text{R}}$ (μs)	2.7 ± 0.5	2.2 ± 2

TABLE I. Summary of device parameters for qubit A and qubit B, respectively.

where $\Delta_{\text{fgge}} = \omega_{\text{d}} - \omega_{\text{fgge}}$ is the detuning between the drive and the fgge transition frequency. After a time $t_g = \pi / \sqrt{g_{\text{fgge}}^2 + (\Delta_{\text{fgge}}/2)^2}$, an initial $|ge\rangle$ state completes one round trip in the fg-ge manifold and accumulates a geometric phase $\phi_{\text{fgge}} = \pi - \Delta_{\text{fgge}} t_g / 2$. From Eq. (C1) we then obtain that the detuning should be set to $\Delta_{\text{fgge}} = -2\chi$.

In the experiment, the coupling g_{fgge} is not turned on and off instantaneously and, moreover, the dispersive coupling is altered during the gate due to the dressing between the drive and the qubit, $\chi = \chi(\Omega_{\text{fgge}})$. As a result, the detuning has to be calibrated and we find an optimal working point at $\Delta_{\text{fgge}}/2\pi = 0.96$ MHz.

[1] A. Blais, A. L. Grimsmo, S. M. Girvin, and A. Wallraff, "Circuit quantum electrodynamics," arXiv:2005.12667 (2020).

[2] Andrew W. Cross, Lev S. Bishop, Sarah Sheldon, Paul D. Nation, and Jay M. Gambetta, "Validating quantum computers using randomized model circuits," Phys. Rev. A **100**, 032328 (2019).

[3] J. S. Otterbach, R. Manenti, N. Alidoust, A. Bestwick, M. Block, B. Bloom, S. Caldwell, N. Didier, E. Schuyler Fried, S. Hong, P. Karalekas, C. B. Osborn, A. Papageorge, E. C. Peterson, G. Prawiroatmodjo, N. Rubin, Colm A. Ryan, D. Scarabelli, M. Scheer, E. A. Sete, P. Sivarajah, Robert S. Smith, A. Staley, N. Tezak, W. J. Zeng, A. Hudson, Blake R. Johnson, M. Reagor, M. P. da Silva, and C. Rigetti, "Unsupervised Machine Learning on a Hybrid Quantum Computer," arXiv:1712.05771 (2017).

[4] Frank Arute, Kunal Arya, Ryan Babbush, Dave Bacon, Joseph C. Bardin, Rami Barends, Rupak Biswas, Sergio Boixo, Fernando G. S. L. Brandao, David A. Buell, Brian Burkett, Yu Chen, Zijun Chen, Ben Chiaro, Roberto Collins, William Courtney, Andrew Dunsworth, Edward Farhi, Brooks Foxen, Austin Fowler, Craig Gidney, Marissa Giustina, Rob Graff, Keith Guerin, Steve Habegger, Matthew P. Harrigan, Michael J. Hartmann, Alan Ho, Markus Hoffmann, Trent Huang, Travis S. Humble, Sergei V. Isakov, Evan Jeffrey, Zhang Jiang, Dvir Kafri, Kostyantyn Kechedzhi, Julian Kelly, Paul V. Klimov, Sergey Knysh, Alexander Korotkov, Fedor Kostritsa, David Landhuis, Mike Lindmark, Erik Lucero, Dmitry Lyakh, Salvatore Mandrà, Jarrod R. McClean, Matthew McEwen, Anthony Megrant, Xiao Mi, Kristel Michielsen, Masoud Mohseni, Josh Mutus, Ofer Naaman, Matthew Neeley, Charles Neill, Murphy Yuezhen Niu, Eric Ostby, Andre Petukhov, John C. Platt, Chris Quintana, Eleanor G. Rieffel, Pedram Roushan, Nicholas C. Rubin, Daniel Sank, Kevin J. Satzinger, Vadim Smelyanskiy, Kevin J. Sung, Matthew D. Trevithick, Amit Vainsencher, Benjamin Villalonga, Theodore White, Z. Jamie Yao, Ping Yeh, Adam Zalcman, Hartmut Neven, and John M. Martinis, "Quantum supremacy using a programmable superconducting processor," Nature **574**, 505–510 (2019).

[5] Morten Kjaergaard, Mollie E. Schwartz, Jochen Braumüller, Philip Krantz, Joel I.-J. Wang, Simon Gustavsson, and William D. Oliver, "Superconducting qubits: Current state of play," Annual Review of Condensed Matter Physics **11**, 369–395 (2020).

[6] Jay M. Gambetta, Jerry M. Chow, and Matthias Steffen, "Building logical qubits in a superconducting quantum computing system," npj Quantum Information **3**, 2 (2017).

[7] R. Barends, C. M. Quintana, A. G. Petukhov, Yu Chen, D. Kafri, K. Kechedzhi, R. Collins, O. Naaman, S. Boixo, F. Arute, K. Arya, D. Buell, B. Burkett, Z. Chen, B. Chiaro, A. Dunsworth, B. Foxen, A. Fowler, C. Gidney, M. Giustina, R. Graff, T. Huang, E. Jeffrey, J. Kelly, P. V. Klimov, F. Kostritsa, D. Landhuis, E. Lucero, M. McEwen, A. Megrant, X. Mi, J. Mutus, M. Neeley, C. Neill, E. Ostby, P. Roushan, D. Sank, K. J. Satzinger, A. Vainsencher, T. White, J. Yao, P. Yeh, A. Zalcman, H. Neven, V. N. Smelyanskiy, and John M. Martinis, "Diabatic gates for frequency-tunable superconducting qubits," Phys. Rev. Lett. **123**, 210501 (2019).

[8] B. Foxen, C. Neill, A. Dunsworth, P. Roushan, B. Chiaro, A. Megrant, J. Kelly, Z. Chen, K. Satzinger, R. Barends, F. Arute, K. Arya, R. Babbush, D. Bacon, J. C. Bardin, S. Boixo, D. Buell, B. Burkett, Y. Chen, R. Collins, E. Farhi, A. Fowler, C. Gidney, M. Giustina, R. Graff, M. Harrigan, T. Huang, S. V. Isakov, E. Jeffrey, Z. Jiang, D. Kafri, K. Kechedzhi, P. Klimov, A. Korotkov, F. Kostritsa, D. Landhuis, E. Lucero, J. McClean, M. McEwen, X. Mi, M. Mohseni, J. Y. Mutus, O. Naaman, M. Neeley, M. Niu, A. Petukhov, C. Quintana, N. Rubin, D. Sank, V. Smelyanskiy, A. Vainsencher, T. C. White, Z. Yao, P. Yeh, A. Zalcman, H. Neven, and J. M. Martinis, "Demonstrating a continuous set of two-qubit gates for near-term quantum algorithms," arXiv:2001.08343 (2020).

[9] M. Kjaergaard, M. E. Schwartz, A. Greene, G. O. Samach, A. Bengtsson, M. O'Keeffe, C. M. McNally, J. Braumüller, D. K. Kim, P. Krantz, P. Marvian, A. Melville, B. M. Niedzielski, Y. Sung, R. Winik, J. Yoder, D. Rosenberg, K. Obenland, S. Lloyd, T. P. Orlando, I. Marvian, S. Gustavsson, and W. Oliver, "A quantum instruction set implemented on a superconducting quantum processor," arXiv:2001.08838 (2020).

[10] L. DiCarlo, J. M. Chow, J. M. Gambetta, Lev S. Bishop, B. R. Johnson, D. I. Schuster, J. Majer, A. Blais, L. Frunzio, S. M. Girvin, and R. J. Schoelkopf, "Demonstration of two-qubit algorithms with a superconducting quantum processor," Nature **460**, 240–244 (2009).

[11] R. Barends, J. Kelly, A. Megrant, A. Veitia, D. Sank, E. Jeffrey, T. C. White, J. Mutus, A. G. Fowler, B. Campbell, Y. Chen, Z. Chen, B. Chiaro, A. Dunsworth, C. Neill, P. O'Malley, P. Roushan, A. Vainsencher, J. Wenner, A. N. Korotkov, A. N. Cleland, and John M. Martinis, "Superconducting quantum circuits at the surface code threshold for fault tolerance," Nature **508**, 500–503 (2014).

[12] Yu Chen, C. Neill, P. Roushan, N. Leung, M. Fang, R. Barends, J. Kelly, B. Campbell, Z. Chen, B. Chiaro, A. Dunsworth, E. Jeffrey, A. Megrant, J. Y. Mutus, P. J. J. O'Malley, C. M. Quintana, D. Sank,

A. Vainsencher, J. Wenner, T. C. White, Michael R. Geller, A. N. Cleland, and John M. Martinis, "Qubit architecture with high coherence and fast tunable coupling," Phys. Rev. Lett. **113**, 220502 (2014).

[13] David C. McKay, Ravi Naik, Philip Reinhold, Lev S. Bishop, and David I. Schuster, "High-contrast qubit interactions using multimode cavity qed," Phys. Rev. Lett. **114**, 080501 (2015).

[14] M. A. Rol, F. Battistel, F. K. Malinowski, C. C. Bultink, B. M. Tarasinski, R. Vollmer, N. Haider, N. Muthusubramanian, A. Bruno, B. M. Terhal, and L. DiCarlo, "Fast, high-fidelity conditional-phase gate exploiting leakage interference in weakly anharmonic superconducting qubits," Phys. Rev. Lett. **123**, 120502 (2019).

[15] David C. McKay, Stefan Filipp, Antonio Mezzacapo, Easwar Magesan, Jerry M. Chow, and Jay M. Gambetta, "Universal gate for fixed-frequency qubits via a tunable bus," Phys. Rev. Applied **6**, 064007 (2016).

[16] S. A. Caldwell, N. Didier, C. A. Ryan, E. A. Sete, A. Hudson, P. Karalekas, R. Manenti, M. P. da Silva, R. Sinclair, E. Acala, N. Alidoust, J. Angeles, A. Bestwick, M. Block, B. Bloom, A. Bradley, C. Bui, L. Capelluto, R. Chilcott, J. Cordova, G. Crossman, M. Curtis, S. Deshpande, T. El Bouayadi, D. Girshovich, S. Hong, K. Kuang, M. Lenihan, T. Manning, A. Marchenkov, J. Marshall, R. Maydra, Y. Mohan, W. O'Brien, C. Osborn, J. Otterbach, A. Papageorge, J.-P. Paquette, M. Pelstring, A. Polloreno, G. Prawiroatmodjo, V. Rawat, M. Reagor, R. Renzas, N. Rubin, D. Russell, M. Rust, D. Scarabelli, M. Scheer, M. Selvanayagam, R. Smith, A. Staley, M. Suska, N. Tezak, D. C. Thompson, T.-W. To, M. Vahidpour, N. Vodrahalli, T. Whyland, K. Yadav, W. Zeng, and C. Rigetti, "Parametrically activated entangling gates using transmon qubits," Phys. Rev. Applied **10**, 034050 (2018).

[17] Pranav Mundada, Gengyan Zhang, Thomas Hazard, and Andrew Houck, "Suppression of qubit crosstalk in a tunable coupling superconducting circuit," Phys. Rev. Applied **12**, 054023 (2019).

[18] P. V. Klimov, J. Kelly, Z. Chen, M. Neeley, A. Megrant, B. Burkett, R. Barends, K. Arya, B. Chiaro, Yu Chen, A. Dunsworth, A. Fowler, B. Foxen, C. Gidney, M. Giustina, R. Graff, T. Huang, E. Jeffrey, Erik Lucero, J. Y. Mutus, O. Naaman, C. Neill, C. Quintana, P. Roushan, Daniel Sank, A. Vainsencher, J. Wenner, T. C. White, S. Boixo, R. Babbush, V. N. Smelyanskiy, H. Neven, and John M. Martinis, "Fluctuations of energy-relaxation times in superconducting qubits," Phys. Rev. Lett. **121**, 090502 (2018).

[19] J. Koch, T. M. Yu, J. Gambetta, A. A. Houck, D. I. Schuster, J. Majer, A. Blais, M. H. Devoret, S. M. Girvin, and R. J. Schoelkopf, "Charge-insensitive qubit design derived from the Cooper pair box," Phys. Rev. A **76**, 042319 (2007).

[20] P. J. Leek, S. Filipp, P. Maurer, M. Baur, R. Bianchetti, J. M. Fink, M. Göppl, L. Steffen, and A. Wallraff, "Using sideband transitions for two-qubit operations in superconducting circuits," Phys. Rev. B **79**, 180511 (2009).

[21] Jerry M. Chow, Jay M. Gambetta, A. D. Córcoles, Seth T. Merkel, John A. Smolin, Chad Rigetti, S. Poletto, George A. Keefe, Mary B. Rothwell, J. R. Rozen, Mark B. Ketchen, and M. Steffen, "Universal quantum gate set approaching fault-tolerant thresholds with superconducting qubits," Phys. Rev. Lett. **109**, 060501 (2012).

[22] S. Poletto, Jay M. Gambetta, Seth T. Merkel, John A. Smolin, Jerry M. Chow, A. D. Córcoles, George A. Keefe, Mary B. Rothwell, J. R. Rozen, D. W. Abraham, Chad Rigetti, and M. Steffen, "Entanglement of two superconducting qubits in a waveguide cavity via monochromatic two-photon excitation," Phys. Rev. Lett. **109**, 240505 (2012).

[23] Jerry M Chow, Jay M Gambetta, Andrew W Cross, Seth T Merkel, Chad Rigetti, and M Steffen, "Microwave-activated conditional-phase gate for superconducting qubits," New J. Phys. **15**, 115012 (2013).

[24] Andrew W. Cross and Jay M. Gambetta, "Optimized pulse shapes for a resonator-induced phase gate," Phys. Rev. A **91**, 032325 (2015).

[25] D.J. Egger, M. Ganzhorn, G. Salis, A. Fuhrer, P. Müller, P.Kl. Barkoutsos, N. Moll, I. Tavernelli, and S. Filipp, "Entanglement generation in superconducting qubits using holonomic operations," Phys. Rev. Applied **11**, 014017 (2019).

[26] Chad Rigetti and Michel Devoret, "Fully microwave-tunable universal gates in superconducting qubits with linear couplings and fixed transition frequencies," Phys. Rev. B **81**, 134507 (2010).

[27] Sarah Sheldon, Easwar Magesan, Jerry M. Chow, and Jay M. Gambetta, "Procedure for systematically tuning up cross-talk in the cross-resonance gate," Phys. Rev. A **93**, 060302(R) (2016).

[28] M. Brink, J. M. Chow, J. Hertzberg, E. Magesan, and S. Rosenblatt, "Device challenges for near term superconducting quantum processors: frequency collisions," *2018 IEEE International Electron Devices Meeting (IEDM)*, IEE , 6.1.1–6.1.3 (2018).

[29] A. D. Córcoles, Jay M. Gambetta, Jerry M. Chow, John A. Smolin, Matthew Ware, Joel Strand, B. L. T. Plourde, and M. Steffen, "Process verification of two-qubit quantum gates by randomized benchmarking," Phys. Rev. A **87**, 030301 (2013).

[30] F. Motzoi, J. M. Gambetta, P. Rebentrost, and F. K. Wilhelm, "Simple pulses for elimination of leakage in weakly nonlinear qubits," Phys. Rev. Lett. **103**, 110501 (2009).

[31] J. M. Chow, L. DiCarlo, J. M. Gambetta, F. Motzoi, L. Frunzio, S. M. Girvin, and R. J. Schoelkopf, "Optimized driving of superconducting artificial atoms for improved single-qubit gates," Phys. Rev. A **82**, 040305 (2010).

[32] J. M. Gambetta, F. Motzoi, S. T. Merkel, and F. K. Wilhelm, "Analytic control methods for high-fidelity unitary operations in a weakly nonlinear oscillator," Phys. Rev. A **83**, 012308–13 (2011).

[33] P. Magnard, P. Kurpiers, B. Royer, T. Walter, J.-C. Besse, S. Gasparinetti, M. Pechal, J. Heinsoo, S. Storz, A. Blais, and A. Wallraff, "Fast and unconditional all-microwave reset of a superconducting qubit," Phys. Rev. Lett. **121**, 060502 (2018).

[34] R. Bianchetti, S. Filipp, M. Baur, J. M. Fink, C. Lang, L. Steffen, M. Boissonneault, A. Blais, and A. Wallraff, "Control and tomography of a three level superconducting artificial atom," Phys. Rev. Lett. **105**, 223601 (2010).

[35] C. Macklin, K. O'Brien, D. Hover, M. E. Schwartz, V. Bolkhovsky, X. Zhang, W. D. Oliver, and I. Siddiqi, "A near-quantum-limited Josephson traveling-wave parametric amplifier," Science **350**, 307–310 (2015).

[36] Yves Salathé, Philipp Kurpiers, Thomas Karg, Christian

Lang, Christian Kraglund Andersen, Abdulkadir Akin, Sebastian Krinner, Christopher Eichler, and Andreas Wallraff, "Low-latency digital signal processing for feedback and feedforward in quantum computing and communication," Phys. Rev. Applied **9**, 034011 (2018).

[37] A. Dewes, F. R. Ong, V. Schmitt, R. Lauro, N. Boulant, P. Bertet, D. Vion, and D. Esteve, "Characterization of a two-transmon processor with individual single-shot qubit readout," Phys. Rev. Lett. **108**, 057002 (2012).

[38] P. Kurpiers, P. Magnard, T. Walter, B. Royer, M. Pechal, J. Heinsoo, Y. Salathé, A. Akin, S. Storz, J.-C. Besse, S. Gasparinetti, A. Blais, and A. Wallraff, "Deterministic quantum state transfer and remote entanglement using microwave photons," Nature **558**, 264–267 (2018).

[39] M. Pechal, L. Huthmacher, C. Eichler, S. Zeytinoğlu, A. A. Abdumalikov Jr., S. Berger, A. Wallraff, and S. Filipp, "Microwave-controlled generation of shaped single photons in circuit quantum electrodynamics," Phys. Rev. X **4**, 041010 (2014).

[40] S. Zeytinoğlu, M. Pechal, S. Berger, A. A. Abdumalikov Jr., A. Wallraff, and S. Filipp, "Microwave-induced amplitude- and phase-tunable qubit-resonator coupling in circuit quantum electrodynamics," Phys. Rev. A **91**, 043846 (2015).

[41] Simone Gasparinetti, Simon Berger, Abdufarrukh A. Abdumalikov, Marek Pechal, Stefan Filipp, and Andreas J. Wallraff, "Measurement of a vacuum-induced geometric phase," Sci. Adv. **2**, e1501732 (2016).

[42] D.J. Egger, M. Werninghaus, M. Ganzhorn, G. Salis, A. Fuhrer, P. Müller, and S. Filipp, "Pulsed reset protocol for fixed-frequency superconducting qubits," Phys. Rev. Applied **10**, 044030 (2018).

[43] Erik Sjöqvist, "Geometric phases in quantum information," International Journal of Quantum Chemistry **115**, 1311–1326 (2015).

[44] David C. McKay, Christopher J. Wood, Sarah Sheldon, Jerry M. Chow, and Jay M. Gambetta, "Efficient z gates for quantum computing," Phys. Rev. A **96**, 022330 (2017).

[45] S. Krinner, S. Lazar, A. Remm, C. K. Andersen, N. Lacroix, G. J. Norris, C. Hellings, M. Gabureac, C. Eichler, and A. Wallraff, "Benchmarking coherent errors in controlled-phase gates due to spectator qubits," arXiv:2005.05914 (2020).

[46] Lorenza Viola and Seth Lloyd, "Dynamical suppression of decoherence in two-state quantum systems," Phys. Rev. A **58**, 2733–2744 (1998).

[47] L. M. K. Vandersypen and I. L. Chuang, "NMR techniques for quantum control and computation," Rev. Mod. Phys. **76**, 1037 (2004).

[48] J. Bylander, S. Gustavsson, F. Yan, F. Yoshihara, K. Harrabi, G. Fitch, D. G. Cory, Y. Nakamura, J.-S. Tsai, and Oliver W. D., "Noise spectroscopy through dynamical decoupling with a superconducting flux qubit," Nat. Phys. **7**, 565–570 (2011).

[49] Qiujiang Guo, Shi-Biao Zheng, Jianwen Wang, Chao Song, Pengfei Zhang, Kemin Li, Wuxin Liu, Hui Deng, Keqiang Huang, Dongning Zheng, Xiaobo Zhu, H. Wang, C.-Y. Lu, and Jian-Wei Pan, "Dephasing-insensitive quantum information storage and processing with superconducting qubits," Phys. Rev. Lett. **121**, 130501 (2018).

[50] J. Ku, X. Xu, M. Brink, D. C. McKay, J. B. Hertzberg, M. H. Ansari, and B. L. T. Plourde, "Suppression of unwanted zz interactions in a hybrid two-qubit system," arXiv:2003.02775 (2020).

[51] S. Rosenblum, P. Reinhold, M. Mirrahimi, Liang Jiang, L. Frunzio, and R. J. Schoelkopf, "Fault-tolerant detection of a quantum error," Science **361**, 266–270 (2018).

[52] J. P. Gaebler, A. M. Meier, T. R. Tan, R. Bowler, Y. Lin, D. Hanneke, J. D. Jost, J. P. Home, E. Knill, D. Leibfried, and D. J. Wineland, "Randomized benchmarking of multiqubit gates," Phys. Rev. Lett. **108**, 260503 (2012).

[53] Easwar Magesan, Jay M. Gambetta, B. R. Johnson, Colm A. Ryan, Jerry M. Chow, Seth T. Merkel, Marcus P. da Silva, George A. Keefe, Mary B. Rothwell, Thomas A. Ohki, Mark B. Ketchen, and M. Steffen, "Efficient measurement of quantum gate error by interleaved randomized benchmarking," Phys. Rev. Lett. **109**, 080505 (2012).

[54] Zijun Chen, Julian Kelly, Chris Quintana, R. Barends, B. Campbell, Yu Chen, B. Chiaro, A. Dunsworth, A. G. Fowler, E. Lucero, E. Jeffrey, A. Megrant, J. Mutus, M. Neeley, C. Neill, P. J. J. O'Malley, P. Roushan, D. Sank, A. Vainsencher, J. Wenner, T. C. White, A. N. Korotkov, and John M. Martinis, "Measuring and suppressing quantum state leakage in a superconducting qubit," Phys. Rev. Lett. **116**, 020501 (2016).

[55] Christian Kraglund Andersen, Ants Remm, Stefania Lazar, Sebastian Krinner, Nathan Lacroix, Graham J. Norris, Mihai Gabureac, Christopher Eichler, and Andreas Wallraff, "Repeated quantum error detection in a surface code," Nature Physics (2020).

[56] P. Kurpiers, M. Pechal, B. Royer, P. Magnard, T. Walter, J. Heinsoo, Y. Salathé, A. Akin, S. Storz, J.-C. Besse, S. Gasparinetti, A. Blais, and A. Wallraff, "Quantum communication with time-bin encoded microwave photons," Phys. Rev. Applied **12**, 044067 (2019).

[57] S. Krinner, S. Storz, P. Kurpiers, P. Magnard, J. Heinsoo, R. Keller, J. Lütolf, C. Eichler, and A. Wallraff, "Engineering cryogenic setups for 100-qubit scale superconducting circuit systems," EPJ Quantum Technology **6**, 2 (2019).

[58] Alexandre Blais, Ren-Shou Huang, Andreas Wallraff, S. M. Girvin, and R. J. Schoelkopf, "Cavity quantum electrodynamics for superconducting electrical circuits: An architecture for quantum computation," Phys. Rev. A **69**, 062320 (2004).

[59] Milena Grifoni and Peter Hänggi, "Driven quantum tunneling," Physics Reports **304**, 229 – 354 (1998).